Somatic mutations and promotor methylation of the ryanodine receptor 2 is a common event in the pathogenesis of head and neck cancer

Katrin Schmitt[1], Britta Molfenter[1], Natalia Koerich Laureano[1,2,3], Bouchra Tawk[4], Matthias Bieg[5], Xavier Pastor Hostench[5], Dieter Weichenhan[6], Nina D. Ullrich[7], Viny Shang[1], Daniela Richter[8], Fabian Stögbauer[9], Lea Schroeder[10], Bianca de Bem Prunes[3], Fernanda Visioli[3], Pantelis Varvaki Rados[3], Adriana Jou[1,2], Michaela Plath[1], Philippe A. Federspil[1], Julia Thierauf[1], Johannes Döscher[11], Stephanie E. Weissinger[12], Thomas K. Hoffmann[11], Steffen Wagner[13], Claus Wittekindt[13], Naveed Ishaque[5], Roland Eils[5], Jens P. Klussmann[14], Dana Holzinger[10], Christoph Plass[6], Amir Abdollahi[4], Kolja Freier[15], Wilko Weichert[16], Karim Zaoui[1]* and Jochen Hess[1,2]*

[1]Department of Otorhinolaryngology, Head and Neck Surgery, Heidelberg University Hospital, Heidelberg, Germany
[2]Molecular Mechanisms of Head and Neck Tumors, German Cancer Research Center (DKFZ), Heidelberg, Germany
[3]Oral Pathology, Federal University of Rio Grande do Sul (UFRGS), Porto Alegre, Brazil
[4]Division of Molecular and Translational Radiation Oncology, Heidelberg Ion Therapy Center (HIT), Heidelberg Institute of Radiation Oncology (HIRO), Heidelberg University Hospital, and Translational Radiation Oncology, German Cancer Consortium (DKTK), National Center for Tumor Diseases (NCT), German Cancer Research Center (DKFZ), Heidelberg, Germany
[5]Division of Theoretical Bioinformatics, German Cancer Research Center (DKFZ), and Heidelberg Center for Personalized Oncology (DKFZ-HIPO), Heidelberg, Germany
[6]Cancer Epigenomics, German Cancer Research Center (DKFZ), Heidelberg, Germany
[7]Institute of Physiology and Pathophysiology, Division of Cardiovascular Physiology, Heidelberg University, Heidelberg, Germany
[8]Translational Medical Oncology, National Center for Tumor Diseases (NCT) Dresden, Dresden and German Cancer Research Center (DKFZ), Heidelberg, Germany
[9]Institute of Pathology, Heidelberg University Hospital, Heidelberg, Germany
[10]Division of Molecular Diagnostics of Oncogenic Infections, Infection, Inflammation and Cancer Program, German Cancer Research Center (DKFZ), Heidelberg, Germany
[11]Department of Otorhinolaryngology, Head and Neck Surgery, University Medical Center Ulm, Ulm, Germany
[12]Institute of Pathology, University Hospital Ulm, Ulm, Germany
[13]Department of Otorhinolaryngology, Head and Neck Surgery, University of Giessen, Giessen, Germany
[14]Department of Otorhinolaryngology, Head and Neck Surgery, University of Cologne, Cologne, Germany
[15]Department of Oral and Maxillofacial Surgery, Heidelberg University Hospital, Heidelberg, Germany
[16]Institute of Pathology, Technical University Munich (TUM), and German Cancer Consortium (DKTK) partner site, Munich, Germany

Genomic sequencing projects unraveled the mutational landscape of head and neck squamous cell carcinoma (HNSCC) and provided a comprehensive catalog of somatic mutations. However, the limited number of significant cancer-related genes obtained so far only partially explains the biological complexity of HNSCC and hampers the development of novel diagnostic biomarkers and therapeutic targets. We pursued a multiscale omics approach based on whole-exome sequencing, global DNA methylation and gene expression profiling data derived from tumor samples of the HIPO-HNC cohort (n = 87), and confirmed new findings with

Key words: DNA methylation, HNSCC, RYR2, head and neck cancer, omics analysis

Abbreviations: DAC: Decitabine; FFPE: formalin fixed paraffin embedded; HIPO: Heidelberg Center for Personalized Oncology; HNC: head and neck cancer; HNSCC: head and neck squamous cell carcinoma; HPV: human papillomavirus; OPSCC: oropharyngeal squamous cell carcinoma; RYR2: ryanodine receptor 2; TCGA: The Cancer Genome Atlas; TSS: transcription start sites

Conflict of interest: All authors declare that they have no conflict of interest.
Grant sponsor: NCT Precision Oncology Program (NCT POP), NCT 3.0_2015.21 NCT-PRO, Coordination of Improvement of Higher Level Personnel (CAPES); **Grant sponsor:** iMED-HNSCC Funding Program of the Helmholtz Initiative on Personalized Medicine; **Grant sponsor:** German Cancer Research Center-Heidelberg Center for Personalized Oncology (DKFZ-HIPO)
*K.Z. and J.H. contributed equally to this work

Correspondence to: Karim Zaoui, MD, Department of Otorhinolaryngology, Head and Neck Surgery, Ruprecht-Karls-University, Im Neuenheimer Feld 400, D-69120 Heidelberg, Germany, Tel.: +49-6221-5639510, Fax: +49-6221-5633654, E-mail: karim.zaoui@med.uni-heidelberg.de

datasets from The Cancer Genome Atlas (TCGA). Promoter methylation was confirmed by MassARRAY analysis and protein expression was assessed by immunohistochemistry and immunofluorescence staining. We discovered a set of cancer-related genes with frequent somatic mutations and high frequency of promoter methylation. This included the ryanodine receptor 2 (RYR2), which showed variable promoter methylation and expression in both tumor samples and cell lines. Immunohistochemical staining of tissue sections unraveled a gradual loss of RYR2 expression from normal mucosa *via* dysplastic lesion to invasive cancer and indicated that reduced RYR2 expression in adjacent tissue and precancerous lesions might serve as risk factor for unfavorable prognosis and upcoming malignant conversion. In summary, our data indicate that impaired RYR2 function by either somatic mutation or epigenetic silencing is a common event in HNSCC pathogenesis. Detection of RYR2 expression and/or promoter methylation might enable risk assessment for malignant conversion of dysplastic lesions.

What's new?

Multi-scale omics approaches provide a powerful tool to unravel cancer-related genes with the potential to serve as prognostic biomarkers and putative drug targets. This study shows that somatic mutations and epigenetic silencing of the ryanodine receptor 2 (RYR2) are frequent in head and neck cancer. Loss of RYR2 expression was found during transition from dysplastic lesions to invasive tumors. Detection of somatic mutations or promoter methylation might thus improve risk assessment of malignant conversion, which could enable timely and adequate treatment of premalignant lesions.

Introduction

Head and neck cancer (HNC) constitutes a heterogeneous group of cancers at the upper aerodigestive tract and is one of the most common malignancies worldwide.[1] In the majority of cases, HNCs are diagnosed as squamous cell carcinoma (HNSCC) originating from the mucosal epithelia of the oral cavity, pharynx or larynx.[2] Cigarette smoking and alcohol abuse are major etiological risk factors for HNSCC, while human papillomavirus (HPV) infection is strongly associated with oropharyngeal cancer risk and prognosis.[3,4]

The standard of care for HNSCC includes surgical excision, radiotherapy and platinum-based chemotherapy, which often cause high morbidity and reduced quality of life.[5] Despite multimodal and aggressive treatment regimens, the overall survival of patients with advanced HNSCC remains low due to the high incidence of treatment resistance resulting *in loco*-regional recurrence or distant metastasis.[6,7] Hence, unraveling cellular and molecular principles of intrinsic or acquired treatment resistance has become a prime target for novel drug discovery and design of more effective therapies.[8,9] Equally important is the identification of key players in the pathogenesis of HNSCC, which could improve risk assessment of early malignant conversion to facilitate timely and adequate treatment of premalignant lesions and pave the way to establish new strategies for prevention.

Genomic sequencing approaches have been conducted to unravel the mutational landscape of HNSCC and to provide a comprehensive catalog of candidate genes responsible for the initiation and progression of HNSCC.[10–12] In addition, global gene expression profiling highlighted aberrant activity of gene regulatory networks and signaling cascades, operating in distinct HNSCC subtypes.[13–15]

A fundamental problem of an increasing sample size for cancer genome studies is the large list of putative candidate genes of which many appear highly suspicious on the basis of their expression pattern, biological function or genomic properties. Most cancer genome studies identified frequent somatic mutations in genes encoding extremely large proteins, such as skeletal or cardiac muscle proteins (e.g., TTN, ryanodine receptor 2 [RYR2] and RYR3), membrane-associated mucins (e.g., MUC16 and MUC4), cytoskeletal dyneins (e.g., DNAH5 and DNAH11) or the neuronal synaptic vesicle protein piccolo (PCLO). New algorithms have been developed to reduce the risk of extensive false-positive findings that overshadow true driver events.[16] However, it is worth noting that the limited number of significant candidate genes or specific mutational hotspots in HNSCC obtained by these tools only partially explains their biological complexity and might hamper the development of novel diagnostic markers and therapeutic targets.[17]

In addition to genomic mutations, the accumulation of epigenetic alterations has been identified as a hallmark of HNSCC. Epigenetic alterations and in particular aberrant DNA methylation of CpG units in the proximity of predicted transcription start sites (TSS) are common features of HNSCC and often result in gene expression silencing and signaling pathway deregulation.[18–20] In many cancers, epigenetic events linked to tumor suppressor gene inactivation through promoter hypermethylation are even more frequent than somatic mutations and could drive neoplastic initiation and malignant progression.[21] So far, only a limited number of studies conducted an integrative approach considering both somatic mutations and gene promoter methylation to unravel new key regulators in the pathogenesis of HNSCC.[22]

Materials and Methods

Patient material

Patients of the Heidelberg Center for Personalized Oncology-Head and Neck Cancer (HIPO-HNC) cohort (n = 87) were treated between 2012 and 2016 at the University Hospital Heidelberg, Germany, and the cohort consists primarily of

advanced HNSCC from the oropharynx (n = 36, 41.4%), oral cavity (n = 22, 25.3%), and laryngeal/hypopharyngeal sites (n = 18, 20.7%, Supporting Information Table S1). Patient samples were obtained under the protocol S-206/2011, approved by the Ethics Committee of Heidelberg University, with written informed consent from all participants. Our study was conducted in accordance with the Declaration of Helsinki. Median age at the time of diagnosis was 61.4 years (range: 39.7–82.5 years), most patients were male (n = 67, 78.2%) and smokers (n = 60, 69%). HPV-related tumors were almost exclusively found in the subgroup of oropharyngeal squamous cell carcinoma (OPSCC; n = 22 out of 36, 61.1%), compared to 5.9% (n = 3 out of 51) in non-OPSCC.

Fresh-frozen specimens and tissue sections from formalin fixed paraffin embedded (FFPE) samples of the HIPO-HNC cohort were provided by the NCT tissue bank at the Institute for Pathology, University of Heidelberg, Germany in accordance with its regulations and the approval of the Ethics Committee of Heidelberg University. Tissue sections of dysplastic lesions and malignant tumors for the validation cohorts were provided by Departments of Otorhinolaryngology from Ulm and Giessen, Germany and Oral Pathology, Federal University of Rio Grande do Sul, Porto Alegre, Brazil (Supporting Information Table S2) after approval by the local Ethics Committees (Ethics votes: 374/13 and 95/15, CEP UFRGS 237.008).

Isolation of analytes

Fresh-frozen tumor samples of the HIPO-HNC cohort were obtained from surgical resection and were evaluated by a pathologist (W.W.) to confirm the diagnosis and to estimate neoplastic cell content. Blood samples were collected prior to surgery. DNA and RNA from tumor specimens and DNA from blood samples were isolated at the central DKFZ-HIPO Sample Processing Laboratory using the AllPrep DNA/RNA/Protein Mini Kit (Qiagen, Hilden, Germany) and the QIAamp DNA Blood Mini QIAcube Kit (Qiagen) according to manufacturer's protocols. Quality control and quantification were conducted using a Qubit 2.0 Fluorometer (Thermo Fisher Scientific, Waltham, MA), the Agilent 2100 Bioanalyzer (Agilent Technologies, Santa Clara, CA), and the NanoDrop spectrophotometer (NanoDrop Technologies, Wilmington, DE).

Whole-exome sequencing and data analysis

Exome capturing was performed using SureSelect Human All Exon in-solution capture reagents version 4 and version 6 (Agilent Technologies) including UTRs and sequencing was carried out with a HiSeq 2500 instrument (Illumina, San Diego, CA). Mapping of paired-end short reads was performed using bwa-aln (version 0.6.2) on the 1,000 genomes project's phase 2 reference sequence (ftp://ftp.1000genomes.ebi.ac.uk/vol1/ftp/technical/reference/phase2_reference_assembly_sequence/hs37d5.fa.gz) including decoy sequences. Afterward, the Picard software (https://broadinstitute.github.io/picard/, version 1.61) was used to mark duplicate reads. Summary on detected high confidence indels and single nucleotide variant (SNVs) is provided as Supporting Information Tables S3 and S4.

Global gene expression profiling

Gene expression profiling was conducted with HumanHT-12 BeadChip arrays (Illumina). Biotin-labeled complementary RNA (cRNA) samples were prepared according to the recommended sample labeling procedure based on the modified Eberwine protocol.[23] In brief, 250–500 ng total RNA was used for cDNA synthesis, followed by an amplification/labeling step to synthesize biotin-labeled cRNA using the Illumina® Total Prep™ RNA Amplification Kit (Life Technologies, Carlsbad, CA) and Biotin-16-UTP (Roche Applied Science, Penzberg, Germany). The cRNA was purified with the Illumina® Total Prep™ RNA Amplification Kit (Life Technologies), following quality control and quantification using the Agilent 2100 Bioanalyzer (Agilent Technologies) and NanoDrop spectrophotometer (NanoDrop Technologies). Microarrays were scanned using an iScan array scanner (Illumina). The raw intensity (IDAT) files were imported into the R environment using the limma package[24] and normalized with the neqc function[25] with default parameters.

Global DNA methylation analysis

DNA concentrations were determined using PicoGreen (Molecular Probes, Eugene, OR) and the quality was confirmed by agarose-gel analysis. Only samples with an average fragment size >3 kb were selected for further analysis. About 500 ng genomic DNA from each sample was bisulfite converted using the EZ-96 DNA Methylation Kit (Zymo Research Corporation, Irvine, CA) according to the manufacturer recommendations. After amplification and enzymatic fragmentation following the instructions in the Illumina Infinium HD Assay Methylation Protocol Guide, samples were applied to Infinium HumanMethylation450 or MethylationEPIC BeadChips (Illumina) and hybridization was performed for 16–24 hr at 48°C. After extension, arrays were fluorescently stained and scanned using an iScan array scanner (Illumina). Data analysis was performed in R studio version 1.1.423 and extraction of beta values was performed using the minfi package version 1.24.0.[26–30]

MassARRAY analysis

Quantitative DNA methylation analysis by matrix-assisted time-of-flight mass spectrometry (MassARRAY, Agena Bioscience, San Diego, CA) was performed as described previously[31] using primers purchased from Sigma-Aldrich and listed in Supporting Information Table S5. We used ClustVis, a freely available web server at http://biit.cs.ut.ee/clustvis/[32] to analyze and to visualize the MassARRAY data from the HIPO cohort and HNSCC cell lines in a numeric data matrix. Hierarchical clustering was used to generate heatmap plots with calculating all pairwise distances and the color gradient gives an overview of the numeric differences between samples. Objects with the smallest distance are

merged in each step. No scaling was applied to rows and columns represent individual samples, which were clustered using Euclidean distance and average linkage.

HPV status

HPV status was determined for all cases by BSGP5+/6+-PCR/MPG and E6*I mRNA detection as described previously.[33] HPV DNA- and RNA-positive cases were considered as HPV-related while all other cases (DNA-negative and DNA-positive but RNA-negative) were considered as non-HPV-related.

The Cancer Genome Atlas-HNC and pan-cancer data analysis

The Cancer Genome Atlas (TCGA)-HNC methylation data as assayed by Illumina 450 K Human Methylation Arrays were downloaded in 2015 from the TCGA data portal (https://tcga-data.nci.nih.gov/tcga) for $n = 279$ patients. Downloaded raw idat files were loaded into R studio version 1.1.423 and preprocessed with minfi version 1.24.0. RYR2 promoter and gene body methylation patterns in normal and tumor samples of 23 TCGA cohorts were analyzed using the MethCNA database (http://cgma.scu.edu.cn/MethCNA/).[34] Level 3 RNAseq data were downloaded as described previously.[35] Raw count data were rlog-transformed using DESeq2 package in R and used for further analysis.[36]

Immunohistochemical staining

IHC staining was performed with the Immunodetection Kit (ImmPRESS HRP Antirabbit, Vector Laboratories, Burlingame, CA), according to manufacturer's instructions. Endogenous peroxidase activity was inactivated by incubation of tissue slides with 3% H_2O_2 for 10 min at room temperature. For antigen unmasking slides were boiled for 10 min in 10 mM Citrate buffer. Immunostaining was performed with the anti-RYR2 antibody (PA5-38329, Thermo Fisher, Waltham, MA) using the DAB peroxidase substrate (Vector Laboratories) and histological staining with hematoxylin was done to visualize tissue architecture. Slides were mounted with Eukitt (Sigma, St Louis, MO). Quantification of the relative number of RYR2-positive cells was done by three independent evaluators based on microscopic inspection and categorized as Score 1: 0% positive, Score 2: 1–33% positive cells, Score 3: 34–66% positive cells and Score 4: ≥67% RYR2 positive cells.

Cell culture experiments

FaDu, Cal27, SCC4, SCC9 and SCC25 cells were purchased from the American Type Culture Collection (ATCC, https://www.lgcstandards-atcc.org/). All cell lines were cultured in Dulbecco's Modified Eagle's Medium (DMEM, Sigma) supplemented with 10% fetal calf serum (Sigma), 2 mM L-glutamine (Sigma) and 50 µg/ml Penicillin–Streptomycin (Sigma) in a humidified atmosphere with 6% CO_2 at 37°C. Cell cultures were routinely screened to exclude mycoplasma contamination (Venor®GeM Classic Mycoplasma Detection Kit; Minerva Biolabs, Berlin, Germany) according to manufacturer's instructions, and authentication was confirmed by the Multiplex Human Cell Line Authentication Test (Multiplexion, Supporting Information Data S1).

Immunofluorescence staining

Cells were seeded on coverslips in 12-well plates (Greiner Bio-One) and were either kept for 48 hr under normal growth conditions or were treated for 72 hr with DMSO or 1 µM Decitabine (DAC; Sigma). Cells were fixed with 4% PFA for 15 min at 4°C, incubated for 30 min in 0.5% Triton X-100 and blocked for 30 min with T-buffer (0.2% Tween 20, 1% BSA in PBS). Cells were incubated for 1 hr at room temperature with the anti-RYR2 antibody (Thermo Fisher, PA5-38329; dilution 1:200 in T-buffer), followed by incubation for 30–60 min with the secondary antibody (Jackson Immuno Research, 111-165-008; dilution 1:200 in T-buffer). Nuclei were visualized with DAPI (Sigma, dilution 1:1000). Coverslips were mounted with VectaMount (Vector Laboratories) and were analyzed by fluorescence microscopy (Olympus BX-50F). Pictures were taken from at least five individual fields per experiment using the Olympus XC30 camera. Cells with a perinuclear and dot-like staining pattern were counted manually as RYR2-positive and divided by the total amount of cells to calculate the relative fraction of RYR2-positive cells.

Quantitative RT-PCR analysis

Total RNA isolation was performed with the RNeasy Mini Kit (Qiagen) following the manufacturer's instructions. For DNase digestion RNase free DNase Set (Qiagen) was used. Quantity and quality of isolated total RNA were determined with the Nanodrop 2000 Spectrophotometer (Thermo Fisher). For cDNA synthesis, RevertAid First Strand cDNA Synthesis Kit (Thermo Fisher) was used. About 1 µl Random Hexamer Primer was added to 1 µg RNA diluted in 11 µl RNAse free water and the mixture was incubated for 5 min at 70°C followed by 5 min at 4°C. Subsequently, 4 µl five times Reaction Buffer, 2 µl 10 mM dNTPs, 1 µl RiboLock RNAse Inhibitor and 1 µl RevertAid Reverse Transcriptase were added and incubated for 60 min at 42°C. Quantitative RT-PCR (RQ-PCR) was performed using 10 ng cDNA and the SYBR Green PCR Mix (Thermo Fisher) in the 7900HT Fast Real-Time PCR System (Applied Biosystems, Foster City, CA) according to manufacturer's instruction. RYR2 primers were purchased from Qiagen (RYR2: QuantiTect Primer Assay, Qiagen) and amplification of LMNB1 was used as an internal reference (LMNB1-For: GCTGCTCCTCAACTATG CTAAGAA; LMNB1-Rev: TTTGACGCCCAGAATCCAC). The cycle of threshold (CT) for RYR2 was normalized to the CT value of LMNB1 using the ΔΔCT method. For each primer, efficiency was determined by a dilution series from 0.01 to 100 ng cDNA from SCC4 cells.

Calcium imaging

About 200,000 SCC4 cells were seeded on 35 mm glass bottom dishes (MatTek) and cultured in DMEM for 2 days. Cells were

loaded with 5 μM of the Ca^{2+}-sensitive fluorophore Fluo-4-AM (Thermo Fisher) for 20 min at room temperature in Tyrode's solution (140 mM NaCl, 5.4 mM KCl, 1.8 mM $CaCl_2$, 1.1 mM $MgCl_2$, 5 mM HEPES, 10 mM Glucose). Cells were washed with fresh solution and left for 10 min for deesterification before taking videos of cell clusters on a confocal microscope (Olympus IX81 Fluoview1000). Using a 60× water immersion objective (1.2 numerical aperture), images were continuously recorded at a resolution of 512x512 pixel and a rate of 2 μs per pixel to collect 100–160 images. Cytosolic Ca^{2+} signals were recorded at resting conditions and during stimulation with 10 mM Caffeine (Sigma) with or without 5 min preincubation with 10 μM Ryanodine (Tocris), a potent RYR2 antagonist. Fluo-4 was excited at 473 nm and emission was collected between 490 and 540 nm. Images and videos were processed with ImageJ.[37] Baseline fluorescence intensity was determined independently for each measurement and after subtraction of Caffeine-induced Ca^{2+} quenching. For each setting, at least three independent areas with more than 50 individual cells in total were examined on single cell level. Relative cytoplasmic Ca^{2+} levels are given in $\Delta F/F_0$, with F_0 as basal Ca^{2+} level at rest after background subtraction.

Bioinformatics and statistical analysis

SNV calling was performed using an in-house developed workflow based on samtools-mpileup. This workflow was also used in the frame of the ICGC PanCancer project and can be accessed *via* the Dockstore webpage (https://dockstore.org/containers/quay.io/pancancer/pcawg-dkfz-workflow).[38–40] In short, the workflow first determines variants in the tumor sample and afterward checks, if these variants are also found in the patient-matched control sample to distinguish somatic from germline calls. Further annotation of the variants was done using publicly available tracks, like 1,000 Genome variants, single nucleotide polymorphisms (dbSNP), repeats and other elements. Functional relevance was assessed using the Annovar software, and the variants were scored for confidence.[41] Small insertions and deletions were obtained from Platypus (version 0.7.4) and further annotated and confidence assessed similarly as in SNV calling.[42]

Mutational significance calculation was done using mutSigCV.[16] PCA analysis and illustration by heatmaps were done with https://biit.cs.ut.ee/clustvis/.[32] Columns are clustered using Euclidean distance and average linkage. Coding non-synonymous SNVs, which were found in the TCGA-HNC and HIPO-HNC cohorts, were analyzed with several algorithms (MutationAssessor,[43] MutationTaster,[44] PolyPhen-2,[45] CADD,[46] SIFT,[47] FATHMM[48,49]) to predict the functional consequence of missense variations. Statistical analysis was done using GraphPad (https://www.graphpad.com/quickcalcs/index.cfm) and IBM SPSS Statistics version 25. p Values <0.05 were considered statistically significant.

Data availability

The data discussed in this publication have been deposited in NCBI's Gene Expression Omnibus (Edgar *et al.*, 2002) and are accessible through GEO Series accession number GSE117973 (https://www.ncbi.nlm.nih.gov/geo/query/acc.cgi?acc=GSE117973) or have been submitted to ArrayExpress (E-MTAB-7478, E-MTAB-7468).

Results

Whole-exome sequencing and global DNA methylation analysis

Whole-exome sequencing data were available for 86 patients of the HIPO-HNC cohort and revealed 28,322 SNVs and 1,969 InDels in total. The highest frequency for somatic mutations was identified for *TP53* in non-HPV-related tumors (75.8%), while only one HPV-related tumor had a *TP53* mutation (Fig. 1*a*). As expected, frequent somatic mutations were found in several genes (e.g., *TTN*, *MUC16*, *PCLO* and *RYR2*) encoding extremely large proteins. Candidate genes with the highest mutational frequency in the HIPO-HNC cohort and a somatic mutation frequency of at least 5% of cases in the TCGA-HNC cohort (n = 510, http://www.cbioportal.org/) were selected for further analysis (Supporting Information Fig. S1).

Gene promoter methylation was assessed by global DNA methylome array analysis and revealed a high beta value (mean and median >0.3) for probes located in the proximity of the predicted TSS for *FAT3*, *TTN*, *MUC16*, *RYR2*, *USH2A*, *PAPPA2*, *NSD1* and *LRP1B* (Fig. 1*b*). DNA methylation and transcript levels for candidate genes with highest beta values were analyzed for samples of the TCGA cohort (n = 279), which confirmed a high correlation for *FAT3*, *MUC16*, *RYR2*, *USH2A*, *PAPPA2* and *LRP1B* (Supporting Information Fig. S2). While high *PAPPA2*, *MUC16* or *FAT3* promoter methylation were positively correlated with their transcript levels, an inverse correlation was detected for *RYR2* or *LRP1B*. In addition, analysis of DNA methylation patterns for normal and tumor samples of the TCGA-HNC cohort by the MethCNA online tool (http://cgma.scu.edu.cn/MethCNA/) demonstrated a prominent difference for probes located at the RYR2 promoter but not in the gene body (Fig. 1*c*). A pan-cancer analysis with 7,731 tumor samples and 741 controls from 23 TCGA cohorts revealed a prominent difference in DNA methylation of probes annotated for the RYR2 promoter but not the gene body (Supporting Information Fig. S3A). A more detailed analysis of cancer cohorts for which DNA methylation data were available for at least n = 20 control samples demonstrated that RYR2 promoter methylation is a common feature for most human cancers analyzed, but is less evident in kidney renal papillary cell carcinoma (TCGA-KIRP), kidney renal clear cell carcinoma (TCGA-KIRC) or thyroid carcinoma (TCGA-THCA). It is worth noting that these cancers are also characterized by a rather low frequency of somatic mutations in RYR2 (Supporting Information Fig. S3C). As observed previously for TCGA-HNC, several cancers including prostate adenocarcinoma (TCGA-PRAD), pancreatic adenocarcinoma (TCGA-PAAD) and cervical cancer (TCGA-CECS) exhibit a highly significant and inverse correlation

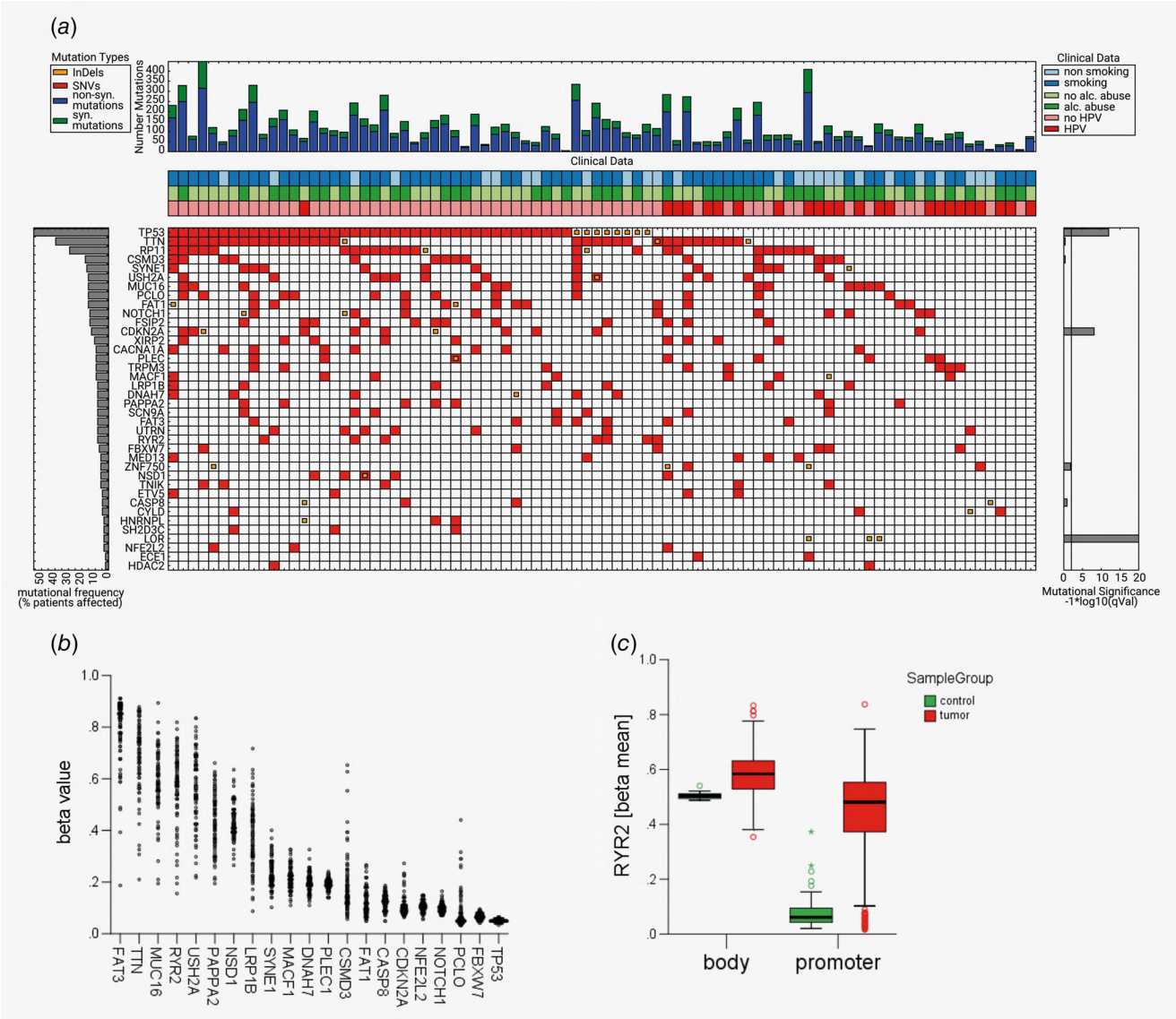

Figure 1. Mutational landscape and gene promoter methylation of the HIPO-HNC cohort. (*a*) Oncomap indicates the number of somatic mutations per sample, etiological risk factors and mutation types of most frequently affected genes based on whole-exome sequencing data of the HIPO-HNC cohort (n = 86). (*b*) The graph summarizes mean beta values of probes in the proximity of annotated transcriptional start sites for most frequently mutated candidate genes in the HIPO-HNC cohort based on global DNA methylation arrays. (*c*) Box plot depicts mean beta values for probes located at the *RYR2* promoter or gene body of normal (green, n = 50) or tumor samples (red, n = 529) from the TCGA-HNC cohort (http://cgma.scu.edu.cn/MethCNA/). [Color figure can be viewed at wileyonlinelibrary.com]

between gene promoter methylation and RYR2 transcript levels (Supporting Information Fig. S3B).

RYR2 promoter methylation and transcription

Inspection of the *RYR2* promoter using the UCSC Genome Browser revealed a well-defined CpG island and three array probes (cg03422911, cg18375860 and cg19764418) are located at its 5′-region (Supporting Information Fig. S4A). MassARRAY analysis based on six amplicons, which were designed to cover most of the CpG island, was conducted to confirm variable DNA methylation for samples of the HIPO-HNC cohort. Mean values of MassARRAY data for Amplicon 1 and 2 were significantly correlated with mean beta values of overlapping array probes (Supporting Information Fig. S4B). Hierarchical clustering based on quantitative MassARRAY data revealed two main clusters of samples with low to moderate (Cluster A1 and A2) or high *RYR2* promoter methylation (Cluster B; Fig. 2*a* and 2*b*). In line with data from control samples of the TCGA-HNC cohort (Fig. 1*c*), samples from normal mucosa (n = 4) revealed a low methylation value and resemble *RYR2* promoter methylation patterns, which were closely related to HNSCC samples of Cluster A1.

As expected, RYR2 transcript levels were significantly reduced in cluster B as compared to Clusters A1 and A2 (Fig. 2*c*). HPV-related tumors were enriched in Clusters A2

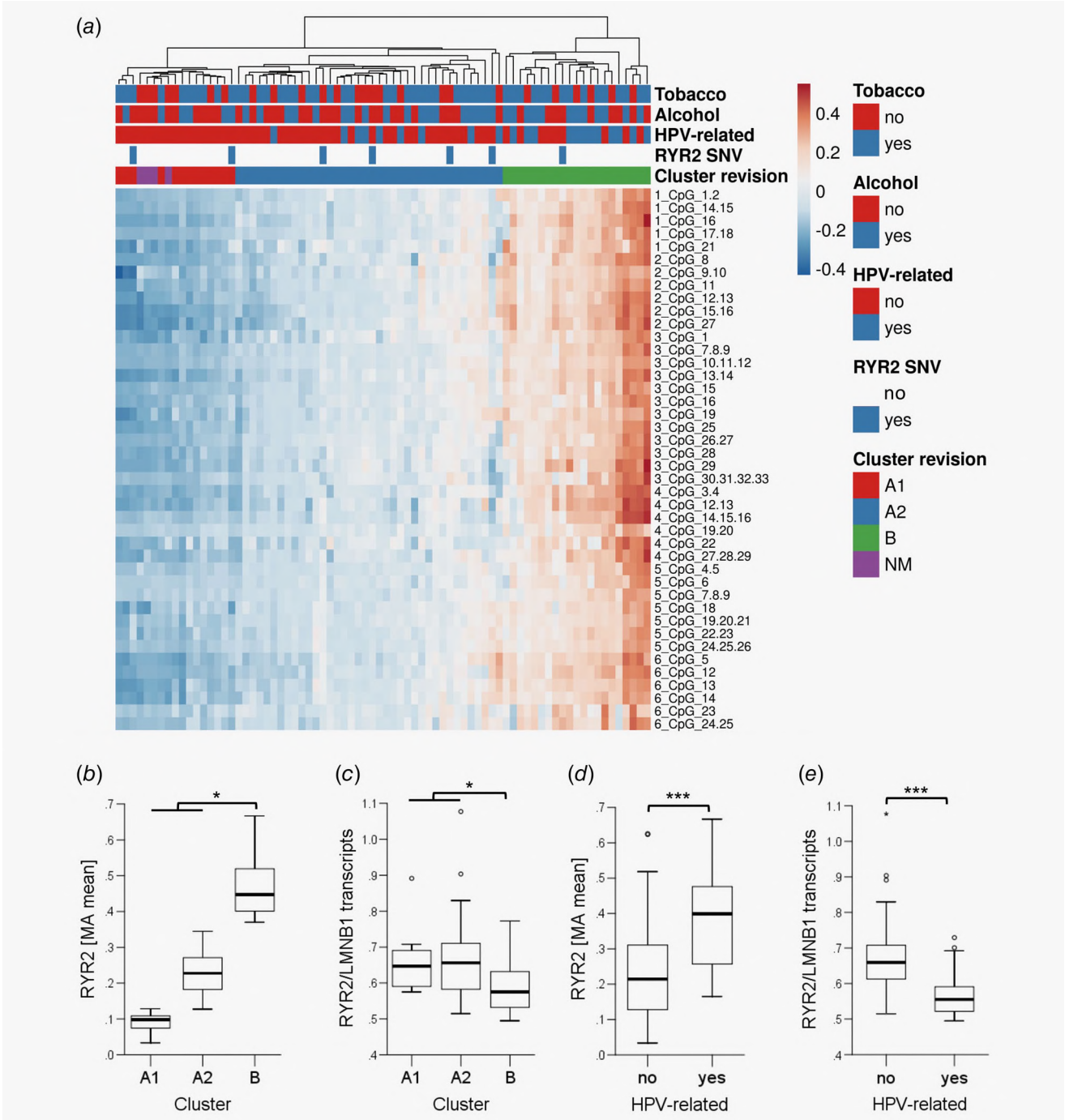

Figure 2. *RYR2* gene promoter methylation and expression in the HIPO-HNC cohort. (*a*) The heatmap was generated by unsupervised hierarchical clustering of MassARRAY data for CpGs (rows) applying Euclidean distance and average linkage on columns (cases of the HIPO-HNC cohort, $n = 72$) and indicates two main clusters (Cluster A and B). Cluster A is further divided into two subclusters A1 and A2. NM, normal mucosa ($n = 4$). Box plots show the distribution of mean MassARRAY values (*b*) and of relative RYR2 transcription normalized to LMNB1 transcript levels (*c*) for samples in cluster A1, A2 and B of the HIPO-HNC cohort as well as the significant differences in *RYR2* promoter methylation (*d*) and transcript levels (*e*) between HPV-related and nonHPV-related tumors. Unpaired *t*-test: **p*-value ‹0.05 and ****p*-value ‹0.0005. [Color figure can be viewed at wileyonlinelibrary.com]

and B, and were completely absent in Cluster A1 (Fig. 2*a*, Supporting Information Table S6). A significantly higher *RYR2* methylation and lower transcript levels were evident in HPV-related as compared to non-HPV-related tumors of the HIPO-HNC cohort (Figs. 2*d* and 2*e*), and was confirmed in the TCGA-HNC cohort (Supporting Information Fig. S5).

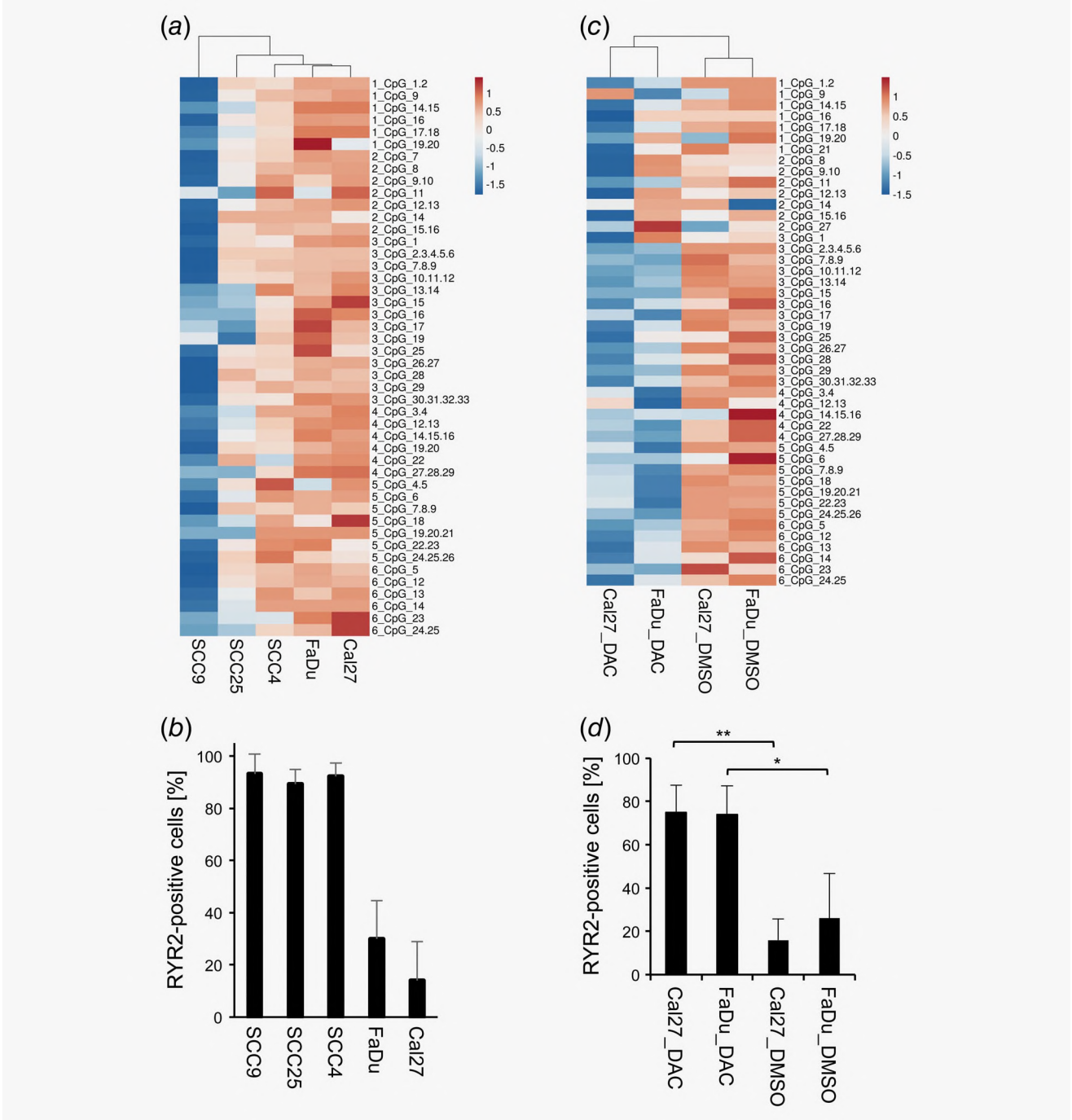

Figure 3. *RYR2* promoter methylation and protein expression in HNSCC cell lines. Heatmaps were generated by unsupervised hierarchical clustering of MassARRAY data for CpGs (rows) applying Euclidean distance and average linkage on columns (HNSCC cell lines) and show differences in *RYR2* promoter methylation for HNSCC cell lines under normal growth conditions (*a*) and upon treatment with Decitabine (DAC) or DMSO as control (*c*). (*b* and *d*) Graphs show the percentage of RYR2-positive cells as determined by IF staining and quantification of five independent fields per cell lines and treatment. Bars represent mean values ± SD of three independent experiments. Unpaired *t*-test:**p*-value ‹0.05 and ***p*-value ‹0.005. [Color figure can be viewed at wileyonlinelibrary.com]

We addressed whether variable *RYR2* promoter methylation and expression also occur in HNSCC cell lines *in vitro*. Genomic DNA from five well-established HNSCC cell lines was evaluated by MassARRAY analysis and *RYR2* promoter methylation was related to protein expression as determined by IF staining (Figs. 3*a* and 3*b*, Supporting Information Fig. S6A). HNSCC cell lines with low to moderate gene promoter methylation (SCC4, SCC9 and SCC25) showed a prominent and perinuclear RYR2 staining pattern in almost all cells, while only a subpopulation of RYR2-positive cells was detected

for those cell lines with gene promoter hypermethylation (FaDu and Cal27). These data suggested a regulation of RYR2 expression by gene promoter methylation in established HNSCC cell lines. Indeed, treatment of FaDu and Cal27 cells with the DNMT-inhibitor DAC increased RYR2 transcript levels and the amount of RYR2-positive cells as compared to DMSO-treated controls (Fig. 3*d*, Supporting Information Figs. S6B and S6C). DAC-induced RYR2 expression was accompanied by demethylation of CpGs in the proximal *RYR2* promoter as determined by MassARRAY analysis (Fig. 3c).

RYR2-related Ca^{2+} release

RYR2 is a major component of the intracellular Ca^{2+} release pathway in cardiomyocytes but is also expressed in nonexcitable cells. To demonstrate RYR2 function in HNSCC cell lines, SCC4 cells with prominent basal RYR2 expression were preloaded with the Ca^{2+}-sensitive fluorophore Fluo-4 and subsequently stimulated with the potent RYR2 agonist Caffeine.[50] Single cell imaging revealed that SCC4 cells exhibit no Ca^{2+} release under control conditions, while Ca^{2+} peaks were detected after Caffeine administration (Supporting Information Figs. S6D and S6E). It is worth noting that the relative amount of SCC4 cells with Caffeine-induced Ca^{2+} release events (86%) coincided with the amount of RYR2-positive cells as determined previously by IF analysis (Fig. 3*b*). Moreover, Caffeine-induced Ca^{2+} release was abolished in most of the analyzed SCC4 cells (98%) upon preincubation with the selective RYR2 inhibitor Ryanodine (Supporting Information Fig. S6F). These data provided compelling experimental evidence that RYR2 is not only expressed but also functions as Ca^{2+} release channel in established HNSCC cell lines.

Loss of RYR2 protein expression during malignant progression

We addressed the question of whether silencing of RYR2 expression becomes evident at a specific time point during HNSCC pathogenesis. FFPE samples of the HIPO-HNC cohort (n = 9) and a cohort of oral cancer patients from Brazil (UFRGS, n = 7) that shared areas of malignant tumor as well as adjacent normal and dysplastic mucosae were selected for IHC staining. IHC staining confirmed a positive RYR2 expression in most keratinocytes of adjacent tissue, while areas of malignant tumors exhibited a more heterogeneous staining pattern ranging from prominent staining in almost all tumor cells to a complete loss of staining (Fig. 4*a*). Most samples also showed a strong staining for stromal cells in the tumor microenvironment most likely representing infiltrating immune cells.

Quantification of the relative amount of RYR2-positive normal and dysplastic keratinocytes or cancer cells, respectively, indicated a gradual decrease of RYR2 expression with dysplasia and an even further reduction in malignant tumors as compared to normal mucosa or dysplastic lesions (Fig. 4*b*). Reduced RYR2 expression in invasive tumors as compared to adjacent dysplastic tissue was further confirmed with matched samples from independent cases of the HIPO-HNC cohort (n = 10), for which no normal mucosa but dysplastic areas were detectable (Fig. 4*c*). In addition, tissue sections from an independent cohort with nonmalignant lesions were analyzed by IHC staining and revealed a RYR2 expression pattern which was similar to adjacent dysplastic tissue of HNSCC (mean score 2.52 $\pm$ 0.88, n = 26). Finally, we identified serial FFPE specimens from two patients, who progressed from a nonmalignant dysplastic lesion to HNSCC over a time period of up to 5 years. Representative pictures of an IHC staining of these samples support a gradual loss of RYR2 expression during malignant progression (Supporting Information Fig. S7).

Although the amount of cases was limited (n = 19), it is worth noting that patients with a reduced RYR2 expression score at the adjacent tissue had a significantly reduced progression-free survival as compared to their counterparts with a normal mucosa-like score (Fig. 4*d*).

Discussion

In our study, we conducted a step-wise approach and unraveled *RYR2* as a candidate gene with a high frequency of somatic mutations and promoter hypermethylation in samples from primary HNC patients. RYR2 is a major component of the intracellular Ca^{2+} release pathway and is associated with the sarcoplasmic or endoplasmic reticulum of several cell types, particularly in cardiomyocytes.[50,51] In cardiomyocytes, RYR2-mediated Ca^{2+} release is crucial for excitation-contraction coupling and mutations in *RYR2* are associated with fatal cardiac arrhythmias and heart failure.[51,52] However, the functional role of RYR2 in nonexcitable cells under physiological and pathological conditions remains controversial.

Although a high *RYR2* mutation frequency is a common feature of numerous human malignancies (Supporting Information Fig. S3C), the relevance of RYR2 in the pathogenesis of cancer has been questioned on the basis of its genomic properties as well as predominant expression and function in cardiomyocytes.[16] Our data indicate that silencing of RYR2 transcription by gene promoter methylation is a common event during HNSCC pathogenesis, but also other human cancers. However, in a substantial amount of cases somatic mutations occur and two findings support the assumption that cancer-related somatic mutations might effect RYR2 protein function: (*i*) coding nonsynonymous SNVs, which were found in the TCGA-HNC and HIPO-HNC cohorts, were analyzed with well-established algorithms (MutationAssessor, MutationTaster, PolyPhen-2, CADD, SIFT and FATHMM) to predict a functional consequence of missense variations. For more than two-thirds of detected missense variations, a damaging or disease-causing consequence with an impact on protein function was predicted by at least 75% of these algorithms (Supporting Information Table S7), and (*ii*) 10 HNC-linked missense variants are also listed in public databases (https://www.ncbi.nlm.nih.gov/clinvar/ and https://databases.lovd.nl/shared/genes/RYR2) and are related to catecholaminergic polymorphic ventricular tachycardia, cardiac

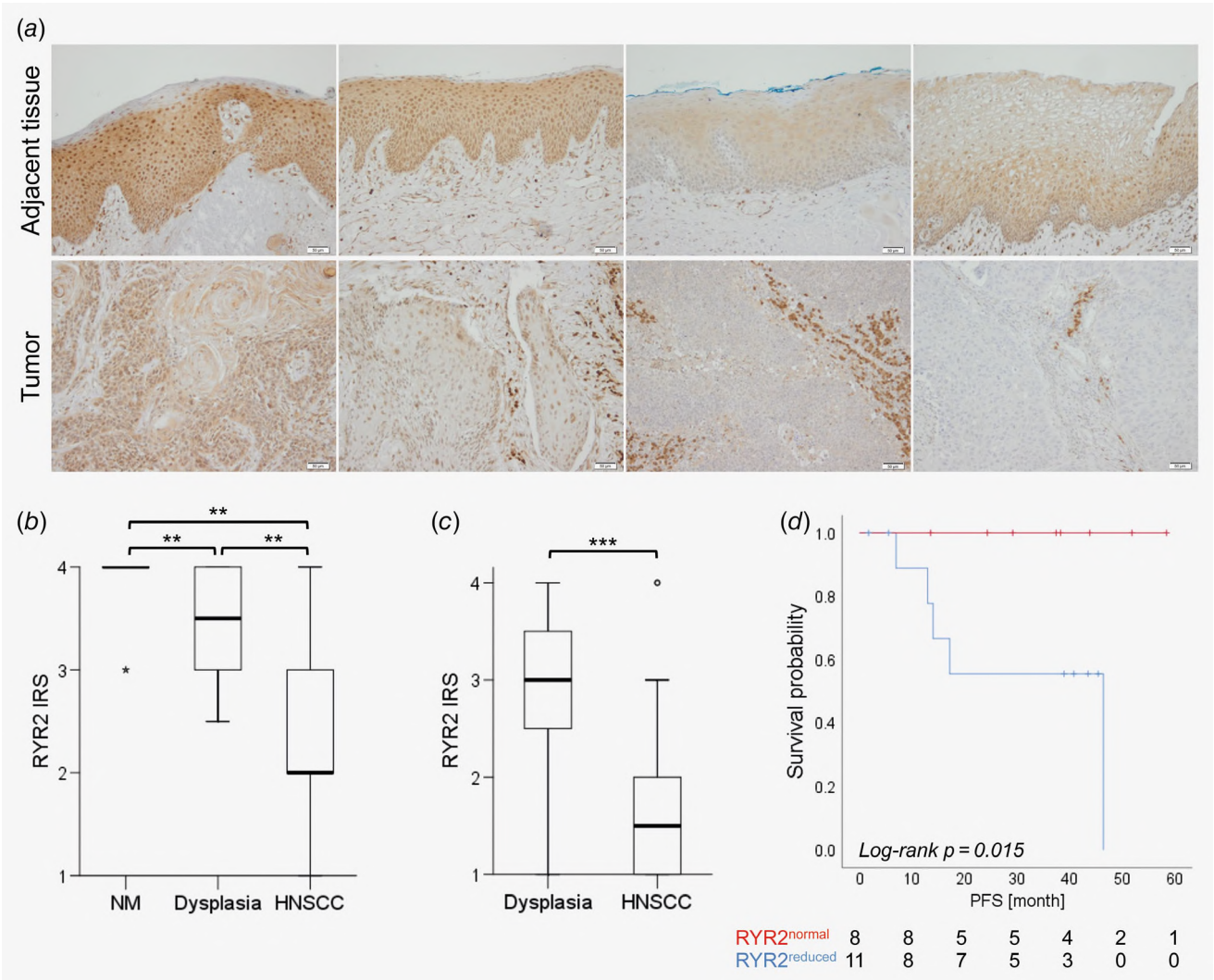

Figure 4. RYR2 expression in normal, dysplastic and malignant tissues. (*a*) Representative pictures of an IHC staining with FFPE tissue sections demonstrate RYR2 expression patterns (brown signal) in adjacent tissue (upper panel) and matched malignant tumor tissue (lower panel) of selected samples from the HIPO-HNC cohort. Box plots summarize the distribution of the RYR2 immunoreactivity score (IRS) as determined by IHC staining of tissue sections from the HIPO-HNC ($n = 9$) and UFRGS ($n = 7$) cohorts with matched areas of normal mucosa, dysplasia and malignant tumor (*b*) or tissue sections from independent cases of the HIPO-HNC ($n = 10$) cohort and validation cohorts ($n = 12$, Ulm and Giessen) with matched areas of dysplasia and malignant tumor (*c*). The RYR2 IRS represents the relative amount of RYR2-positive keratinocytes or tumor cells from absent (1) to ≥67% (4). (*d*) Kaplan–Meier graph shows a significant difference in progression-free survival (PFS) between subgroups of patients with normal (IRS = 4, red line) or reduced RYR2 expression (IRS < 4, blue line) in adjacent tissue. Numbers below the graph represent patients at risk at the indicated time points. Wilcoxon test: ***p*-value <0.005, ****p*-value <0.0005. [Color figure can be viewed at wileyonlinelibrary.com]

arrhythmia or cardiovascular phenotype. For some of these missense variants, experimental data confirm their impact on RYR2 function. As an example, the missense mutation R176Q which is associated with arrhythmogenic right ventricular dysplasia type 2 causes structural alterations which are linked to channel dysfunction.[53] In a mouse knock-in model, the R176Q mutation predisposes the heart to catecholamine-induced oscillatory calcium-release events that trigger a calcium-dependent ventricular arrhythmia.[54]

Our data suggest a potential role of RYR2-dependent Ca^{2+} signaling in differentiation and tissue homeostasis, which is supported by the fact that RYR2 was detected by Denda *et al.*[55] in epidermal keratinocytes with increased expression in differentiating as compared to proliferative keratinocytes *in vitro*. Ca^{2+} imaging after agonist and antagonist treatment indicated that RYR2 is not only expressed but also functional in a HNSCC cell line with prominent basal RYR2 expression as it is in epidermal keratinocytes.[55] Altered RYR2 activity either due to somatic mutation or epigenetic silencing might impair differentiation and thereby might accelerate malignant progression of transformed keratinocytes in combination with other oncogenic events. In line with this assumption, *RYR2*

promoter methylation is common in HPV-driven tumors, which are often characterized by a nonkeratinizing and basaloid histopathology as well as the absence of detectable premalignant dysplastic lesions.[56]

So far, only a few studies addressed RYR2 regulation and function in epithelial tumor cells. RYR2 expression and Caffeine-stimulated Ca^{2+} release were reported for prostate and breast cancer cell lines.[57,58] Mariot *et al.*[59] provided experimental data that a RYR-related Ca^{2+} mobilization augments apoptosis of LNCaP cells, a RYR1- and RYR2-positive prostate cancer cell line. In contrast, a strong RYR2 up-regulation was found in a breast cancer cell line upon EGF-induced epithelial-to-mesenchymal transition,[58] a process which is related with a higher risk for tumor cell dissemination and treatment failure in many epithelial malignancies, including HNSCC.[60] These controversial findings indicate a context-dependent function of RYR2 in epithelial and tumor cells derived thereof, and it will be a major challenge in future studies to unravel underlying molecular principles by loss-of-function and gain-of-function approaches.

IHC staining of tissue sections demonstrated a gradual loss of RYR2 protein expression from adjacent normal mucosa *via* dysplastic lesions to cancer, which is most likely due to an increase in promoter methylation. Our findings raise the attractive question, whether reduced RYR2 expression and/or an increase of promoter methylation in premalignant lesions of the head and neck region could serve as diagnostic biomarkers to assess the risk of malignant conversion and to facilitate timely and adequate treatment. This issue remains an unmet medical need of high clinical relevance,[61] but a large collection of premalignant tissue samples from patients with or without subsequent diagnosis of HNSCC will be required to finally answer this question. Moreover, reduced RYR2 expression in adjacent tissue of primary HNSCC served as a risk factor for shorter progression-free survival. Low RYR2 expression may indicate the presence of altered keratinocyte differentiation due to genetic and/or epigenetic changes in the field surrounding the tumor. The concept of field cancerization, which is attributed to premalignant fields surrounding the primary tumor, has been shown to drive the high rate of local recurrence in HNSCC,[62,63] and molecular studies have provided compelling experimental evidence that the majority of HPV-negative HNSCC, but also other epithelial cancers, develop within local fields of premalignant cells that are clonally related to the resected primary cancer.[64] However, the samples size in our study was limited and the potential association between low RYR2 expression in tumor adjacent tissue and field cancerization or premalignant field requires further confirmation in a larger prospective study.

Acknowledgements

We are grateful to Marion Bähr, Oliver Mücke, Barbara Schwager, Claudia Rittmüller, Antje Schuhmann and Nataly Henfling for excellent technical assistance, and thank Christina Geörg, Bettina Meissburger, Katrin Pfütze (Center for Personalized Oncology - DKFZ-HIPO, Heidelberg, Germany) as well as Melanie Bewerunge-Hudler and Angela Schulz (Core Facility Genomics & Proteomics, DKFZ Heidelberg, Germany) for providing excellent services. We thank the tissue bank of the National Center for Tumor Disease (Institute of Pathology, University Hospital Heidelberg, Germany) for providing paraffin-embedded tumor specimens. This work was supported by the German Cancer Research Center-Heidelberg Center for Personalized Oncology (DKFZ-HIPO), the NCT Precision Oncology Program (NCT POP), NCT 3.0_2015.21 NCT-PRO, Coordination of Improvement of Higher Level Personnel (CAPES) and the iMED-HNSCC Funding Program of the Helmholtz Initiative on Personalized Medicine.

References

1. Ferlay J, Soerjomataram I, Dikshit R, et al. Cancer incidence and mortality worldwide: sources, methods and major patterns in GLOBOCAN 2012. *Int J Cancer* 2015;136:E359–86.
2. Leemans CR, Snijders PJF, Brakenhoff RH. The molecular landscape of head and neck cancer. *Nat Rev Cancer* 2018;18:269–82.
3. Castellsague X, Alemany L, Quer M, et al. HPV involvement in head and neck cancers: comprehensive assessment of biomarkers in 3680 patients. *J Natl Cancer Inst* 2016;108:djv403.
4. Gillison ML, Chaturvedi AK, Anderson WF, et al. Epidemiology of human papillomavirus-positive head and neck squamous cell carcinoma. *J Clin Oncol* 2015;33:3235–42.
5. Ringash J. Survivorship and quality of life in head and neck cancer. *J Clin Oncol* 2015;33:3322–7.
6. Chinn SB, Myers JN. Oral cavity carcinoma: current management, controversies, and future directions. *J Clin Oncol* 2015;33:3269–76.
7. Sacco AG, Cohen EE. Current treatment options for recurrent or metastatic head and neck squamous cell carcinoma. *J Clin Oncol* 2015;33:3305–13.
8. Hedberg ML, Goh G, Chiosea SI, et al. Genetic landscape of metastatic and recurrent head and neck squamous cell carcinoma. *J Clin Invest* 2016;126:169–80.
9. Kang H, Kiess A, Chung CH. Emerging biomarkers in head and neck cancer in the era of genomics. *Nat Rev Clin Oncol* 2015;12:11–26.
10. Agrawal N, Frederick MJ, Pickering CR, et al. Exome sequencing of head and neck squamous cell carcinoma reveals inactivating mutations in NOTCH1. *Science* 2011;333:1154–7.
11. Stransky N, Egloff AM, Tward AD, et al. The mutational landscape of head and neck squamous cell carcinoma. *Science* 2011;333:1157–60.
12. Cancer Genome Atlas Network. Comprehensive genomic characterization of head and neck squamous cell carcinomas. *Nature* 2015;517:576–82.
13. Keck MK, Zuo Z, Khattri A, et al. Integrative analysis of head and neck cancer identifies two biologically distinct HPV and three non-HPV subtypes. *Clin Cancer Res* 2015;21:870–81.
14. Wichmann G, Rosolowski M, Krohn K, et al. The role of HPV RNA transcription, immune response-related gene expression and disruptive TP53 mutations in diagnostic and prognostic profiling of head and neck cancer. *Int J Cancer* 2015;137:2846–57.
15. Linge A, Lock S, Gudziol V, et al. Low cancer stem cell marker expression and low hypoxia identify good prognosis subgroups in HPV(−) HNSCC after postoperative radiochemotherapy: a multicenter study of the DKTK-ROG. *Clin Cancer Res* 2016;22:2639–49.
16. Lawrence MS, Stojanov P, Polak P, et al. Mutational heterogeneity in cancer and the search for new cancer-associated genes. *Nature* 2013;499:214–8.
17. Hammerman PS, Hayes DN, Grandis JR. Therapeutic insights from genomic studies of head and neck squamous cell carcinomas. *Cancer Discov* 2015;5:239–44.
18. Koffler J, Sharma S, Hess J. Predictive value of epigenetic alterations in head and neck squamous cell carcinoma. *Mol Cell Oncol* 2014;1:e954827.
19. Lleras RA, Smith RV, Adrien LR, et al. Unique DNA methylation loci distinguish anatomic site and HPV status in head and neck squamous cell carcinoma. *Clin Cancer Res* 2013;19:5444–55.
20. Brennan K, Koenig JL, Gentles AJ, et al. Identification of an atypical etiological head and neck squamous carcinoma subtype featuring the CpG Island methylator phenotype. *EBioMedicine* 2017;17:223–36.
21. Rodriguez-Paredes M, Esteller M. Cancer epigenetics reaches mainstream oncology. *Nat Med* 2011;17:330–9.

22. Guerrero-Preston R, Michailidi C, Marchionni L, et al. Key tumor suppressor genes inactivated by "greater promoter" methylation and somatic mutations in head and neck cancer. *Epigenetics* 2014;9:1031–46.
23. Eberwine J, Spencer C, Miyashiro K, et al. Complementary DNA synthesis in situ: methods and applications. *Methods Enzymol* 1992;216:80–100.
24. Ritchie ME, Phipson B, Wu D, et al. Limma powers differential expression analyses for RNA-sequencing and microarray studies. *Nucleic Acids Res* 2015;43:e47.
25. Shi W, Oshlack A, Smyth GK. Optimizing the noise versus bias trade-off for Illumina whole genome expression BeadChips. *Nucleic Acids Res* 2010;38:e204.
26. Aryee MJ, Jaffe AE, Corrada-Bravo H, et al. Minfi: a flexible and comprehensive bioconductor package for the analysis of Infinium DNA methylation microarrays. *Bioinformatics* 2014;30:1363–9.
27. Triche TJ Jr, Weisenberger DJ, Van Den Berg D, et al. Low-level processing of Illumina Infinium DNA methylation BeadArrays. *Nucleic Acids Res* 2013;41:e90.
28. Fortin JP, Triche TJ Jr, Hansen KD. Preprocessing, normalization and integration of the Illumina HumanMethylationEPIC array with minfi. *Bioinformatics* 2017;33:558–60.
29. Fortin JP, Labbe A, Lemire M, et al. Functional normalization of 450k methylation array data improves replication in large cancer studies. *Genome Biol* 2014;15:503.
30. R Studio Team. *RStudio: Integrated Development for R*. Boston, MA. Available from: http://www.rstudio.com/: RStudio, Inc., 2015.
31. Ehrich M, Nelson MR, Stanssens P, et al. Quantitative high-throughput analysis of DNA methylation patterns by base-specific cleavage and mass spectrometry. *Proc Natl Acad Sci USA* 2005;102:15785–90.
32. Metsalu T, Vilo J. ClustVis: a web tool for visualizing clustering of multivariate data using principal component analysis and heatmap. *Nucleic Acids Res* 2015;43:W566–70.
33. Halec G, Holzinger D, Schmitt M, et al. Biological evidence for a causal role of HPV16 in a small fraction of laryngeal squamous cell carcinoma. *Br J Cancer* 2013;109:172–83.
34. Deng G, Yang J, Zhang Q, et al. MethCNA: a database for integrating genomic and epigenomic data in human cancer. *BMC Genomics* 2018;19:138.
35. Tawk B, Schwager C, Deffaa O, et al. Comparative analysis of transcriptomics based hypoxia signatures in head- and neck squamous cell carcinoma. *Radiother Oncol* 2016;118:350–8.
36. Love MI, Huber W, Anders S. Moderated estimation of fold change and dispersion for RNA-seq data with DESeq2. *Genome Biol* 2014;15:550.
37. Schneider CA, Rasband WS, Eliceiri KW. NIH image to ImageJ: 25 years of image analysis. *Nat Methods* 2012;9:671–5.
38. Jones DT, Hutter B, Jager N, et al. Recurrent somatic alterations of FGFR1 and NTRK2 in pilocytic astrocytoma. *Nat Genet* 2013;45:927–32.
39. Jones DT, Jager N, Kool M, et al. Dissecting the genomic complexity underlying medulloblastoma. *Nature* 2012;488:100–5.
40. Stein LD, Knoppers BM, Campbell P, et al. Data analysis: create a cloud commons. *Nature* 2015;523:149–51.
41. Wang K, Li M, Hakonarson H. ANNOVAR: functional annotation of genetic variants from high-throughput sequencing data. *Nucleic Acids Res* 2010;38:e164.
42. Rimmer A, Phan H, Mathieson I, et al. Integrating mapping-, assembly- and haplotype-based approaches for calling variants in clinical sequencing applications. *Nat Genet* 2014;46:912–8.
43. Reva B, Antipin Y, Sander C. Predicting the functional impact of protein mutations: application to cancer genomics. *Nucleic Acids Res* 2011;39:e118.
44. Schwarz JM, Cooper DN, Schuelke M, et al. MutationTaster2: mutation prediction for the deep-sequencing age. *Nat Methods* 2014;11:361–2.
45. Adzhubei IA, Schmidt S, Peshkin L, et al. A method and server for predicting damaging missense mutations. *Nat Methods* 2010;7:248–9.
46. Rentzsch P, Witten D, Cooper GM, et al. CADD: predicting the deleteriousness of variants throughout the human genome. *Nucleic Acids Res* 2019;47:D886–D94.
47. Sim NL, Kumar P, Hu J, et al. SIFT web server: predicting effects of amino acid substitutions on proteins. *Nucleic Acids Res* 2012;40:W452–7.
48. Shihab HA, Rogers MF, Gough J, et al. An integrative approach to predicting the functional effects of non-coding and coding sequence variation. *Bioinformatics* 2015;31:1536–43.
49. Shihab HA, Gough J, Cooper DN, et al. Predicting the functional, molecular, and phenotypic consequences of amino acid substitutions using hidden Markov models. *Hum Mutat* 2013;34:57–65.
50. Van Petegem F. Ryanodine receptors: allosteric ion channel giants. *J Mol Biol* 2015;427:31–53.
51. Lanner JT, Georgiou DK, Joshi AD, et al. Ryanodine receptors: structure, expression, molecular details, and function in calcium release. *Cold Spring Harb Perspect Biol* 2010;2:a003996.
52. Chen W, Wang R, Chen B, et al. The ryanodine receptor store-sensing gate controls Ca2+ waves and Ca2+−triggered arrhythmias. *Nat Med* 2014;20:184–92.
53. Amador FJ, Kimlicka L, Stathopulos PB, et al. Type 2 ryanodine receptor domain a contains a unique and dynamic alpha-helix that transitions to a beta-strand in a mutant linked with a heritable cardiomyopathy. *J Mol Biol* 2013;425:4034–46.
54. Kannankeril PJ, Mitchell BM, Goonasekera SA, et al. Mice with the R176Q cardiac ryanodine receptor mutation exhibit catecholamine-induced ventricular tachycardia and cardiomyopathy. *Proc Natl Acad Sci USA* 2006;103:12179–84.
55. Denda S, Kumamoto J, Takei K, et al. Ryanodine receptors are expressed in epidermal keratinocytes and associated with keratinocyte differentiation and epidermal permeability barrier homeostasis. *J Invest Dermatol* 2012;132:69–75.
56. Chakravarthy A, Henderson S, Thirdborough SM, et al. Human papillomavirus drives tumor development throughout the head and neck: improved prognosis is associated with an immune response largely restricted to the oropharynx. *J Clin Oncol* 2016;34:4132–41.
57. Kobylewski SE, Henderson KA, Eckhert CD. Identification of ryanodine receptor isoforms in prostate DU-145, LNCaP, and PWR-1E cells. *Biochem Biophys Res Commun* 2012;425:431–5.
58. Davis FM, Parsonage MT, Cabot PJ, et al. Assessment of gene expression of intracellular calcium channels, pumps and exchangers with epidermal growth factor-induced epithelial-mesenchymal transition in a breast cancer cell line. *Cancer Cell Int* 2013;13:76.
59. Mariot P, Prevarskaya N, Roudbaraki MM, et al. Evidence of functional ryanodine receptor involved in apoptosis of prostate cancer (LNCaP) cells. *Prostate* 2000;43:205–14.
60. Thierauf J, Veit JA, Hess J. Epithelial-to-Mesenchymal transition in the pathogenesis and therapy of head and neck cancer. *Cancers (Basel)* 2017;9:E76.
61. Mehanna HM, Rattay T, Smith J, et al. Treatment and follow-up of oral dysplasia—a systematic review and meta-analysis. *Head Neck* 2009;31:1600–9.
62. Ryser MD, Lee WT, Ready NE, et al. Quantifying the dynamics of Field Cancerization in tobacco-related head and neck cancer: a multiscale Modeling approach. *Cancer Res* 2016;76:7078–88.
63. Leemans CR, Braakhuis BJ, Brakenhoff RH. The molecular biology of head and neck cancer. *Nat Rev Cancer* 2011;11:9–22.
64. Tabor MP, Brakenhoff RH, van Houten VM, et al. Persistence of genetically altered fields in head and neck cancer patients: biological and clinical implications. *Clin Cancer Res* 2001;7:1523–32.